High-performing, linearly controllable electrochemical actuation of *c*-disordered δ-MnO_2/Ni Actuators

Wenrui Ma, K.W. Kwan¶, R. Wu, A.H.W. Ngan

Department of Mechanical Engineering, The University of Hong Kong, Pokfulam Road, Hong Kong, P.R. China

¶ Corresponding author (email: kkwkwan@connect.hku.hk)

Abstract:

Electrochemical actuating materials that can generate mechanical motions in response to low voltage stimuli are useful as artificial muscles in micro- or insect-scale robots. However, such materials tend to have small actuation strain and stress, slow actuation response rate, poor motion controllability, and they often require alkaline electrolytes to operate. Here, we demonstrate and analyse the electrochemical actuation properties of *c*-disordered δ-MnO_2 due to a volume-changing pseudo-capacitive redox reaction, with outstanding actuation performance and maneuverability in the neutral electrolyte of Na_2SO_4. An electrochemo-mechanical model well describes quantitatively the intrinsic actuation properties of δ-MnO_2 and the bending motion of bilayered cantilever actuators comprising an active layer of δ-MnO_2 supported by a Ni thin-film substrate. Under the potential drive between -0.2 and 0.8 V vs SCE in Na_2SO_4, δ-MnO_2 exhibits an electrochemical driving force of $(5.39 \pm 0.40) \times 10^{-23}$ J and activation volume of $(6.26 \pm 0.40) \times 10^{-31}$ m^3 for the actuation at 298 K, a maximum strain of 1.28% and actuation stress of 71.5 MPa, and maximum energy density of 2.76 MJ/m^3, indicating its high potential to be utilized as strong artificial muscles in multi-functional miniaturized actuating devices.

Keywords: bilayered actuator, linearly-controllable, electrochemical actuation, pseudocapacitance, δ-MnO_2

Introduction

Artificial muscles made from stimuli-responsive actuating materials are being intensively explored as prime movers for micro-robotic applications, to replace bulky motors and engines, owing to their advantages including small size, light weight, high sensitivity, good processability and maneuverability[1–3]. Such materials can respond to external stimuli including heat[4,5], light[6–9], humidity[10–12], applied voltage[13,14] and electrochemical potential[15–18] to give rise to certain mechanical motions that depend on the device design. Among them, electrochemical actuators can transfer electrical energy into mechanical energy under low voltage stimuli. Conducting polymers can actuate under the voltage of several volts, but the actuation rate is slow, due to an ion diffusion process within the polymer[19–21]. Nanoporous noble metals[22–24], carbon nanotubes[25–27] and graphene sheets[28–30]are also found to actuate electrochemically under potentials of around 1 V via a non-faradaic electric double layer charge-discharge process, but the strains are small and the fabrication steps are rather complicated. Recently, transition-metal oxides/hydroxides have been established as novel electrochemical actuating materials[7,16–18,31–33]. In particular, the redox couple $Ni(OH)_2$/NiOOH (abbreviated as NHO) were found to actuate in response to a potential window below 1 V in alkaline environments with an actuation strain of ~0.16%[16,18,31] owing to a volume change accompanying the redox reactions, but since the latter happen at rather specific potentials, the actuation has little controllability in terms of magnitude and speed. Cobalt oxides/hydroxides (COH)[34] and nickel-

doped cobalt oxides/hydroxides (CNH)[32], which were studied primarily as light responsive actuating materials, were also reported to actuate moderately under small electrochemical potential signals[6,32]. Tunnel structured ε-MnO_2 was observed to actuate steadily in a neutral electrolyte of Na_2SO_4 within the potential window of 1 V by means of pseudo-capacitive redox reactions[17], and this material is inexpensive to produce and nontoxic for biomedical applications (compared to the NHO and CNH systems). However, the actuation strain of ε-MnO_2 is quite small at 0.1%[17], and so an enhancement in actuation magnitude and controllability is highly desirable for its practical use. As proposed previously, electrochemical actuation is closely related to the charge storage ability of the actuating material[18,22,31,35,36]. The layered type δ-MnO_2, also known as birnessite, possesses better electrochemical capacitance properties compared with other manganese oxides, owing to its large interplanar channels (~0.7 nm) which facilitate fast and reversible intercalation/deintercalation of guest ions along with the faradaic transition of Mn^{3+}/Mn^{4+} [37,38]. Thus, δ-MnO_2 was broadly investigated as a battery[37,39–42] and pseudocapacitor material[43–45]. However, to the best of our knowledge, the actuation capability of δ-MnO_2 under electrochemical stimuli has not been studied before. Therefore, in this work, we investigate the actuation performances of δ-MnO_2/Ni actuators under different potential variation modes below 1 volt in the neutral electrolyte of Na_2SO_4. Furthermore, we employ an electrochemo-mechanical model to quantitatively characterize the intrinsic actuation properties of δ-MnO_2, as well as the actuation performance of the δ-MnO_2/Ni actuators. The results clearly reveal the outstanding electrochemical actuation properties of δ-MnO_2 with good maneuverability, as a promising candidate for developing small, compact electrochemical robotic devices.

Experimental

Materials and Chemicals:

Fluorine-doped tin oxide (FTO) glass (2.3 mm thick, sheet resistance ≈ 10 Ω sq^{-1}) was purchased from Sigma-Aldrich, copper tape was purchased from 3M, and chemical-resist stickers were from MAX Bepop. Nuclepore Track-Etched Polycarbonate membranes with a pore size of 1 μm (micro-porous polycarbonate, or MPPC, membranes) were purchased from Whatman. Deionized (DI) water with resistance higher than 18 MΩ·cm was used for preparing electroplating solutions and actuating electrolyte and rinsing.

A commercial Ni-plating kit (Caswell Inc.) was used for the electroplating of Ni. Oromerse SO Part B (Technic Inc.) plating solution was used for Au electrodeposition. Manganese acetate ($Mn(CH_3COOH)_2$) and sodium sulfate (Na_2SO_4), which were used for the synthesis of manganese oxides, and sodium sulphite (Na_2SO_3), which was used to form the Au plating bath, were purchased from Sigma-Aldrich, without further purification.

Preparation of the actuators:

δ-MnO_2/Ni electrochemical actuators were fabricated through three steps of electrochemical deposition by using a LK2006A electrochemical workstation (Lanlike). First, FTO glass was cut into the size of 50 mm by 25 mm, and rectangular openings with the size of 25 mm by 2.5 mm were shaped on the surface by chemical-resist stickers and an oil marking pen. After rinsed by DI water and dried in hot air flow, a smooth and shiny Ni layer could be electroplated at the openings on the FTO glass in a two-electrode electrochemical cell, under a constant current density of -15 mA/cm^2 for 5 min, against a Ni sheet counter electrode. Subsequently, a thin layer of Au was formed on top of Ni under a constant current density of -0.2 mA/cm^2 for 30

min, against a platinum mesh counter electrode, in a mixed solution of Oromerse SO Part B and 1.7 M Na_2SO_3 in a volume ratio of 1:9. Before the last step of electroplating, a small area at one end of the samples was painted by an oil marking pen, in order to facilitate the subsequent peeling off and attachment processes, as well as to standardize the actuating material plating area to be 20 mm by 2.5 mm. Then, a δ-MnO_2 actuating layer was electroplated on the Au-Ni substrate in a mixed solution of 0.1 M $Mn(CH_3COOH)_2$ and 0.1 M Na_2SO_4. A three-electrode cell was adopted and a constant current density of 0.5 mA/cm^2 was applied, against a saturated calomel reference electrode (SCE) and a platinum mesh counter electrode. Different thicknesses of the δ-MnO_2 actuating layer could be obtained by setting different electroplating time. After each electroplating process, the sample adhered to FTO glass was rinsed by DI water and dried in hot air flow. Finally, the thin-film strip actuator was carefully peeled off and attached to a copper tape, for the subsequent electrochemical actuation tests. Also, two actuators devices were fabricated for demonstration. The fish hook bilayer actuator was fabricated by electrodepositing the δ-MnO_2 actuating material on top of an Au sputtered MPPC substrate. The accordion-like linear actuator was fabricated by three steps of electrodeposition. A Ni thin film was first electrodeposited on the FTO glass. Then the Ni film was peeled off from the FTO glass for Au electrodeposition on both sides. Afterwards, a permanent marker pen was used to paint alternating strips on one side of Au-Ni-Au film, and on the other side, the strips were painted at where it is not painted on the first side. Then the actuating material was electroplated on the area without ink covering, on both sides of the Au-Ni-Au film. The samples were fabricated using the same electroplating solutions and fabrication parameters as mentioned above, and rinsed by DI water and dried in hot air flow after each electroplating processes. Lastly, they were adhered to a copper tape for the electrochemical actuation tests.

Characterization of δ-MnO_2 electrochemical actuator

Thicknesses of Ni Substrate and Au layer were measured by a DektakXT® stylus profiler (Bruker). Material analytical techniques including scanning electron microscopy (SEM), transmission electron microscopy (TEM), X-ray diffraction (XRD) and X-ray photoelectron spectroscopy (XPS) were used for characterization. A Hitachi S4800 FEG scanning electron microscope was used for imaging the surface morphologies and cross-sections of the actuators, as well as for energy dispersive X-ray (EDX) analysis. An FEI Tecnai G^2 20 S-TWIN STEM was used for TEM imaging and selected area electron diffraction (SAED) analysis. The δ-MnO_2 actuating material was prepared and scratched off from the substrate and stuck onto a formvar film for TEM analysis. A Rigaku SmartLab 9-kW X-ray diffractometer was used for GIXRD analysis. Oxidized and reduced XRD samples were prepared by applying 0.8 V and -0.2 V respectively vs SCE in 0.5 M Na_2SO_4 for 30 min to samples on FTO glasses, which were then directly put onto the specimen stage for XRD tests. The incident angle was set as 0.5° and a monochromatic Cu Kα source (λ =1.5406 Å) was used. A Kratos Axis Ultra Spectrometer with a monochromatic Al Kα source was used for XPS analysis.

Electrochemical quartz crystal microbalance (EQCM) measurements

δ-MnO_2 was electroplated on a piece of Au-plated quartz crystal disk with a current density of 0.5 mA/cm^2 for 30 min. Then, the resonant frequency changes (Δf) of the crystal together with the electrochemical data were recorded using a CHI430B electrochemical quartz crystal microbalance (CH Instruments Inc.). The data of frequency changes were converted to mass changes (Δm) of the quartz crystal using the Sauerbrey equation[46]:

$$\Delta f = -2f_0^2 \Delta m/(A\sqrt{\mu\rho}) \quad (1)$$

where $f_0 = 8$ MHz is the fundamental resonant frequency, $A = 0.196$ cm^2 is the area of the Au disk on the quartz crystal, $\mu = 2.95 \times 10^{11}$ g/(cm $\cdot$ s^2) is the shear modulus of the crystal, and $\rho = 2.648$ g/cm^3.

Electrochemical actuation tests and measurements

All the electrochemical actuation tests were conducted with a three-electrode setup (against a saturated calomel reference electrode (SCE) and a platinum mesh counter electrode) using a CHI 660E (CH Instruments) electrochemical workstation. During the test, the actuators were immersed in 0.5 M Na_2SO_4 solution in a transparent container, and the actuation process was recorded by a digital camera (Panasonic Lumix DMC-LX10). The number of forward (positive) and backward (negative) actuation curling loops n_o and n_r were counted from the videos, and the actuation angle magnitudes were calculated as $\theta = 360(n_o - n_r)$. The actuation curvatures κ_o and κ_r were calculated as $\kappa_o = 2n_o\pi/L$ and $\kappa_r = 2n_r\pi/L$, respectively, where L is the length of the actuating material deposited area.

Results and discussion

Characterization of the actuators

The δ-MnO_2/Ni electrochemical actuators comprise three individual layers (Fig. 1a), achieved by three steps of electrodeposition. A Ni thin film of thickness 1.35 ± 0.15 μm was first electrodeposited onto FTO glass to serve as the passive substrate for the actuator. In order to prevent the dissolution of Ni in the subsequent electrodeposition of MnO_2, as well as to improve the adhesion between the MnO_2 actuating layer and the Ni substrate, an ultrathin layer (~200 nm) of Au was electroplated on top of Ni. Then, a layer of black actuating material, which was later identified as Na-incorporated δ-MnO_2, was then electrodeposited on top of the

Au-Ni substrate in static solution without stirring. Different thicknesses of the actuating layer with high uniformity were fabricated by controlling the electroplating time ranging from 5 min to 40 min (Fig S1). Finally, the actuators were carefully peeled off from the FTO glass and adhered to copper tapes at one end for actuation tests. Fig. 1b shows different morphologies of the δ-MnO_2/Ni actuator in air and in a solution of 0.5 M Na_2SO_4. In the as-fabricated state after retracted from the electrodeposition solution and peeled off from the FTO glass, the actuator curls significantly towards the actuating layer in dry air, probably due to the loss of water contents in the actuating material, but on immersion in 0.5 M Na_2SO_4 without applying an electrical potential voltage, it curls in the opposite direction. Such different macroscopic geometric forms show the excellent deformability of the actuator. Surface morphologies and cross-sectional microstructures of the actuators were revealed using scanning electron microscopy (SEM). The Au intermediate layer exhibits a nano-flaked surface morphology (Fig. S2) which greatly enhances the adhesion between the δ-MnO_2 actuating layer and the smooth Ni substrate. From Fig. 1c and 1d, the δ-MnO_2 electrodeposited on top of the Au-Ni support layer has a dense microstructure with interconnected nano-whiskers[47]. The triple layered structure of the actuator is identified by energy-dispersive X-ray spectroscopy (EDS) mapping in Fig. S3. The glazing incidence X-ray diffraction (GIXRD) pattern of the as-prepared actuating material (Fig. 1e) shows only two broad peaks around 37° and 66°, reflecting the poor crystallinity of the actuating material. The two peaks can be matched to the (100) and (110) reflections of δ-MnO_2[42,48–51], with interplanar spacings $d_{100} \approx 0.24$ nm and $d_{110} \approx 0.14$ nm. The ratio of the d values is close to $\sqrt{3}$, indicating a hexagonal layered structure[52]. The asymmetry at the high-angle side of the 37° peak is typical of phyllomanganates with turbostratic disorder[53,54]. Noticeably, compared with the JCPDS data (No. 13-0105) for birnessite, the characteristic diffraction peaks (001) and (002) for the basal planes at around 12° and 25° are totally indistinguishable, indicating a high degree of stacking disorder of the edge-

sharing MnO_6 octahedra sheets[50,52]. Water and metallic cations are often accommodated at the interlayers, stabilizing the negatively-charged MnO_6 octahedra sheets[55]. The EDS result (Fig. S3) also confirms the homogenous distribution of sodium in the as-synthesized active layer. Transmission electron microscope (TEM) image (Fig. 1f) shows a highly crumpled microstructure of the actuating material. Multiple stacked layers lacking long-range ordering can be clearly seen from the high-resolution TEM image (Fig. S4). The interplanar spacing is measured to be 0.62 nm, which is slightly smaller than the theoretical value of 0.7 nm. This might be due to the intercalated water loss during vacuum-pumping before the TEM examination [55,56]. The corresponding selected area electron diffraction (SAED) (Fig. S5) shows two blurry diffraction rings, corresponding to interplanar spacings of 0.24 nm and 0.14 nm, in good match with the aforementioned XRD results. The XPS results in Fig. 1g also confirm the existence of Na in the actuating layer. As displayed in Fig. 1h, the binding energies of Mn $2p_{3/2}$ and Mn $2p_{1/2}$ are 642.3 and 654 eV, respectively, with an energy gap of 11.7 eV, in agreement with birnessite-type MnO_2 in previous studies[57–59]. The Mn 2p spectra can be deconvolved into four peaks, namely, doublet peaks at 641.8 and 653.3 eV for the Mn^{3+} species[60,61], and those at 642.5 and 654.1 eV for the Mn^{4+} species[60,62], as shown in Table S1. The percentages of Mn^{4+} and Mn^{3+} are therefore obtained from the areas of the deconvolved peaks to be 75.3% and 24.7%, respectively, giving the average oxidation state (AOS) of Mn species to be 3.75.

Therefore, the as-synthesized actuating material is confirmed to be δ-MnO_2 with Na^+ ions and water molecules accommodated within the *c*-disordered layers of edge-sharing MnO_6 octahedra, as shown in Fig. 1i.

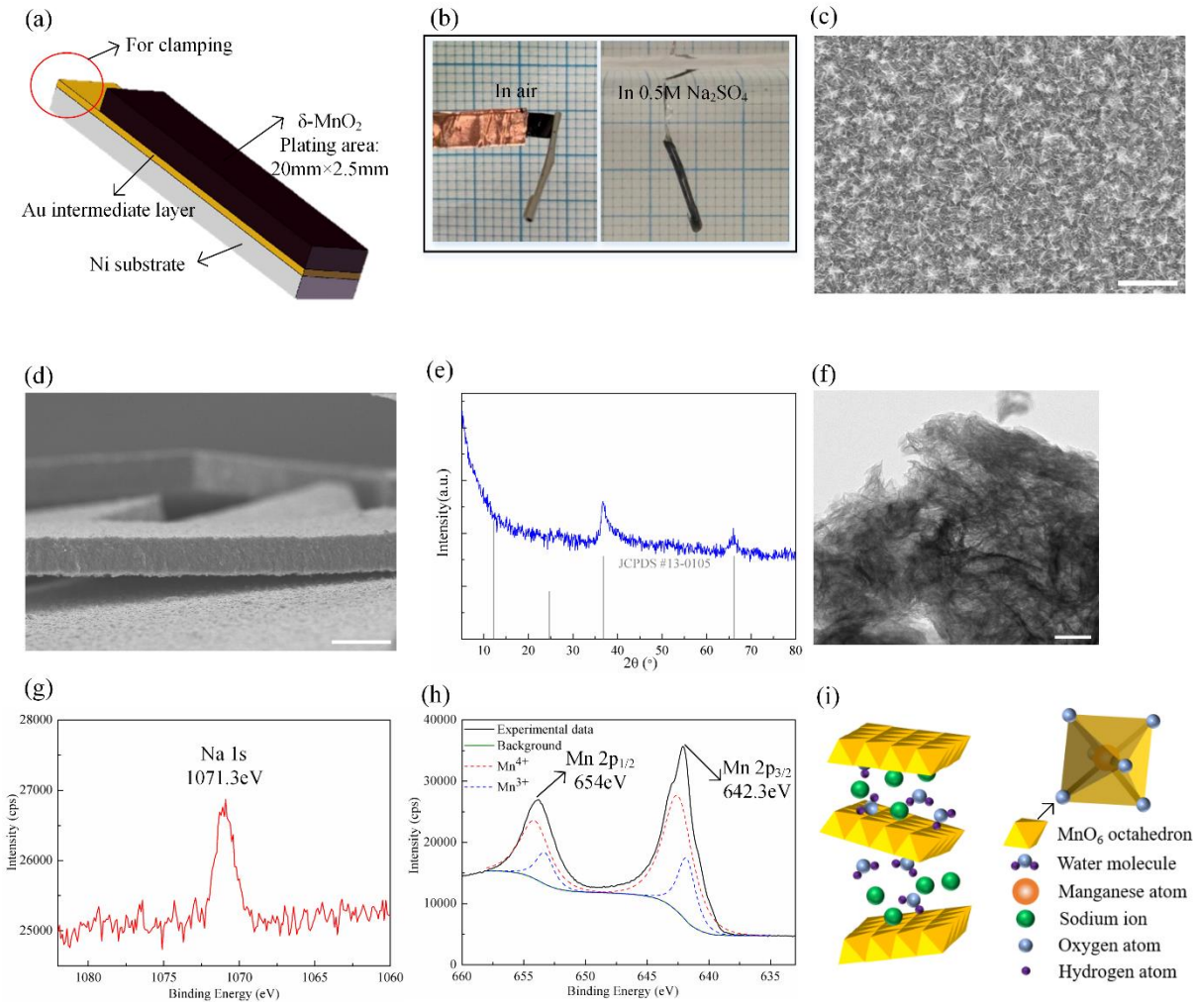

Fig. 1 (a) Schematic of δ-MnO_2/Ni actuator. (b) Snapshots of actuators in air and in the electrolyte of 0.5 M Na_2SO_4. (c, d) SEM image of δ-MnO_2 on top view (c) and cross-section (d) (Scale bar: 5 μm). (e) GIXRD for as-synthesized δ-MnO_2, in comparison with JCPDS data for birnessite. (f) TEM image of as-synthesized δ-MnO_2 (Scale bar: 50 nm). (g, h) XPS spectra of Na 1s (g) and Mn 2p (h). (i) Schematic of the disordered crystal structure of the as-synthesized δ-MnO_2.

Actuation performance of the actuators

To investigate the actuation properties, actuators in strip forms with an MnO_2 area of 20 mm by 2.5 mm fabricated by 20 min electrodeposition were tested under different electrochemical

conditions. Fig. 2a shows the setup for the electrochemical actuation tests: the actuator adhered to a copper tape at one end was connected to the working electrode (WE) of an electrochemical workstation and immersed in 0.5 M Na_2SO_4 electrolyte with a platinum mesh counter electrode (CE), and a saturated calomel electrode (SCE) as the reference electrode (RE). Different electrochemical signals were transmitted to the actuator sample and actuation response of the sample was recorded accordingly by a camera. The typical actuation response of the sample when the potential jumps from -0.2 to 0.8 V vs SCE is shown in Fig. 2b (Video S1, Supporting Information). At the potential of -0.2 V, the actuator curls into multiple helical loops with δ-MnO_2 on the outer side (defined as backward loops and designated as negative). Once the potential jumps to 0.8 V, an extremely large and fast response happens, in which the actuator straightens in ~1.1 s and curls reversely into helical loops with δ-MnO_2 at the inner side (defined as forward loops and designated as positive). When the potential switches back to -0.2 V, the reverse motion takes place as shown in Fig. S3. Fig. 2c shows how the actuation angle changes over time under such step-potential jumps. Upon the potential switch, the actuator responds at a fast rate (> 1700° /s) in the first 2 seconds, followed by a slowed-down motion. Besides, the actuation speed and magnitude of the actuator can be manipulated by altering the potential scan rate and range. Fig. 2d shows the actuation magnitude and speed at different potential scan rates (u) from 0.01 V/s to 1 V/s under cyclic voltammetry, and Fig. 2e shows the corresponding voltammograms (CV). Note that the CVs exhibit near-rectangular shapes for u < 0.2 V/s, which are the typical characteristic of an ideal pseudocapacitor, signifying a relatively steady current flow within the whole potential window. Correspondingly, the actuator actuates at a relatively uniform speed in response to the potential scanning (Fig. S7). Under this circumstance, a higher potential scan rate could offer a higher instantaneous overpotential to increase the ion diffusion rates at the actuator-electrolyte interface and inside the actuating layer, so as to enhance actuation speed of the actuator. On the other hand, the

actuation magnitude improves significantly by lowering the potential scan rate, as the actuator has longer time to react to the electrochemical stimuli and fulfil the ion exchange with electrolyte. Noticeably, under the fast scan rate of 1 V/s, the actuation magnitude is about 4.4 loops in total (forward plus backward loops), corresponding to the actuation angle magnitude of about 1584°, and the actuation motion is accomplished within 1 second. The largest actuation angle magnitude is 3780° under the scan rate of 0.01 V/s. For pseudo-capacitive charge transfer for which the kinetics is limited by ionic diffusion in the electrolyte, according to the Randles–Sevcik equation[63,64], the peak current of the CV is proportional to the square root of scan rate. Owing to the expected proportionality between the charge transfer and the actuation, the current should be proportional to the actuation speed *v*, and hence we found that for $u \geqslant 0.4$ V/s, *v* is proportional to the square root of scan rate ($u^{1/2}$), as shown by the blue line and the blue symbols framed in Fig. 2f. Considering that the actuation angle magnitude θ is related to the average actuation speed v and the period of one cycle T by $\theta = vT/2$, the actuation angle magnitude θ should be proportional to the reciprocal of the square of scan rate $u^{-1/2}$, as shown by the red line and the red symbols framed in Fig. 2f. However, as the scan rate further slows down ($u^{-1/2}$ getting larger), the proportionality for either $1/v$ or θ with $u^{-1/2}$ is not maintained and θ tends towards a steady value. Under this circumstance, the actuation magnitude or speed is no longer controlled by ionic diffusion in the electrolyte, but the thermodynamics of the electrochemical reaction itself, as explained later. Fig. 2g shows the actuation magnitude and average speed within different potential scan windows (0.1↔0.5 V, 0↔0.6 V, -0.1↔0.7 V and -0.2↔0.8 V) at the same scan rate of 0.05 V/s. The actuation angle magnitude increases almost linearly with the width of potential scan window, while the average actuation speed remains constant with little fluctuations within 147 and 168.3°/s. In Fig. 2h, the CVs of the actuator show near-rectangular shapes within different potential windows, indicating that the electrochemical process proceeds at a steady rate. Accordingly, the actuator

actuates steadily within different potential windows, as shown in Fig. S8. The results in Figs. 2g and h indicate that the present δ-MnO_2 actuators are rather linearly controllable, namely, the actuation magnitude changes almost linearly with the applied potential, in stark contrast with other counterpart materials such as NHO[16], COH[6] or CNH[32],which exhibit sharply peaked or irregular CV characteristics, so that actuation and recovery occur unevenly within the potential window, corresponding to multiple oxidation and reduction reactions at rather specific potentials. Also, a δ-MnO_2/Ni actuator was cyclically actuated between 0 and 0.6 V at the scan rate of 0.1 V/s for 3000 cycles, and the actuation angle magnitude shows mild fluctuations with an overall slowly decreasing trend, as shown in Fig. 2i. The actuation magnitude falls to 78% of its original value after 3000 cycles (Video S2, Supporting Information), with the area of the CV, which indicates the charge storage capability of the actuator, decreasing to 66% of its original value, as shown in Fig. 2j. However, the surface morphology of δ-MnO_2 and the active layer-substrate interface show no significant changes after 3000 cycles of actuation, as shown in Fig. S9. Thus, the decrease in actuation magnitude is probably due to the irreversible structural change of δ-MnO_2 after long-term cycling[65,66], fatigue of the actuating material, cracks formation and propagation in the active layer and partial dissolution of Mn species into the electrolyte[67–69]. On the other hand, the actuation angle range, marked by the pink band in Fig. 2i, drifts slowly to the forward curling direction with positive actuation angle values, probably due to the charge accumulation in δ-MnO_2 during long-term cycling at a relatively fast scan rate.

All in all, the actuator displays a fast response with a large magnitude under an electrochemical potential window within 1 V vs SCE, and the actuation performance, namely, actuation magnitude and speed, are rather linearly controllable by adjusting the potential scan rate and range as shown in Figs. 2d and 2g.

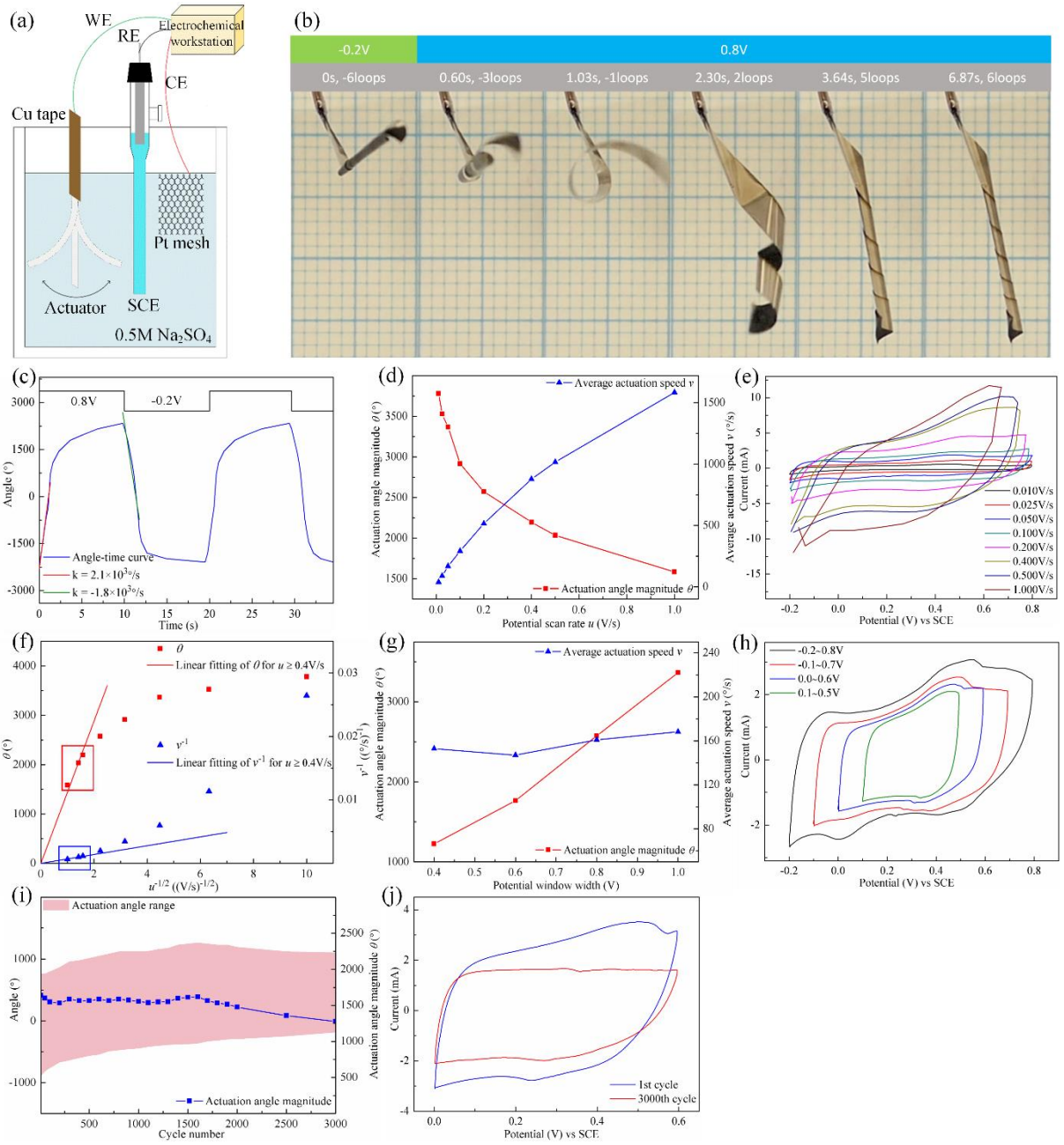

Fig. 2 (a) Schematic of Electrochemical actuation test set-up. (b) Snapshots of actuation response when the potential switches from -0.2 to 0.8 V. (c) Actuation angle plotted against time under step potential of -0.2 and 0.8 V. Black curve shows the potential-time graph. (d) Actuation angle magnitude θ and average actuation speed v plotted against potential scan rate u between -0.2 and 0.8 V. (e) CVs of δ-MnO_2/Ni actuator with different potential scan rates between -0.2 and 0.8 V. (f) θ and v^{-1} plotted against $u^{-1/2}$ with linear fitting for $u \geq 0.4$ V/s. (g) Actuation angle magnitude θ and average actuation speed v plotted against potential window width between at scan rate of 0.05 V/s. (h) CVs of δ-MnO_2/Ni

actuator within different potential scan windows at scan rate of 0.05 V/s. (i) Actuation cyclability performance of δ-MnO_2/Ni actuator. (j) CVs for the 1st and 3000th cycle of δ-MnO_2/Ni actuator.

Actuation mechanism of δ-MnO_2

As shown in Fig. 2b, the actuator exhibits forward curling upon oxidation and backward curling upon reduction. Such a mechanical response is due to the mismatch in length between Au-Ni substrate and δ-MnO_2 layer. As neither electrical current nor mechanical motion could be observed for the Au-Ni substrate under potential scanning (Fig. S10), the actuation is evidently due to a volumetric change of the δ-MnO_2 actuating layer under such conditions. In other words, the δ-MnO_2 layer contracts during anodic scanning and expands during cathodic scanning, which cause the corresponding curling motion of the actuator. As from previous studies on the MnO_2 material system, two charge storage mechanisms of MnO_2 as a pseudocapacitor material have been proposed[70–72]. The first is based on adsorption of electrolyte cations onto the MnO_2 surface:

$$(MnO_2)_{surface} + C^+ + e^- \rightleftharpoons (MnOO^-C^+)_{surface}$$

where C^+ represents electrolyte cations such as Na^+, K^+, Li^+ and H_3O^+. The second involves intercalation of hydrated protons and metallic cations into the bulk of MnO_2 lattice:

$$MnO_2 + C^+ + e^- \rightleftharpoons MnOOC$$

Although a detailed picture of the interplay between electrolyte cations and the layered birnessite electrode material remains ambiguous, it has been proven that electrolyte cations such as Na^+ and H^+ in hydrated and dehydrated states could move into/out of the interlayer regions of MnO_6 octahedra sheets during electrochemical scanning in a neutral aqueous electrolyte such as Na_2SO_4[43]. Besides, reduction of Mn from the +4 to +3 states could induce

Jahn-Teller distortion of the MnO_6 octahedra, with lengthening of Mn-O bonds along certain orbitals [17,44]. On the other hand, the interlayer distance of MnO_6 octahedra sheets expands slightly during oxidation and contracts during reduction due to electrostatic force variation, as proposed previously [43,73], but it cannot be observed for our actuating material, due to the highly disorder along the c-axis.

To verify the actuation mechanism of the δ-MnO_2 actuators we first use electrochemical quartz crystal microbalance (EQCM) to monitor the mass variations during the charging/discharging process. Fig. 3a shows 5 cycles of the CV of δ-MnO_2 in 0.5 M Na_2SO_4 aqueous electrolyte in the window -0.1 ↔ 0.9 V versus Ag/AgCl; the highly overlapped near-rectangular shapes clearly indicate the pseudocapacitive behavior of δ-MnO_2 with excellent reversibility. Such current response is ascribed to the fast and continuous transition of Mn^{3+}/Mn^{4+} couple during potential scanning. The mass change of δ-MnO_2 electrode was recorded concurrently and is shown in Fig. 3b. During the positive potential sweep, the δ-MnO_2 electrode exhibits a gradual decrease in mass, which is recovered to almost the initial value after the reverse sweep. The slight loss in mass after each cycle might be due to the sluggishness of the reduction reaction, namely the incomplete re-intercalation of solution species during negative potential sweep[66] and Mn dissolution into the electrolyte at far negative potentials[44,74]. Highly similar mass-potential curves were observed for the following cycles. The mass change with electrical charge accumulation is plotted in Fig. 3c, and the good linearity between the two parameters indicates the fast and steady intercalation/de-intercalation of electrolyte ions during the potential scanning, in good agreement with the steady actuation motion in response to the potential scanning. The mass-to-charge ratio (MCR) of the δ-MnO_2 electrode, which means the mass gain caused by reduction or mass loss caused by oxidation by 1mol of electrons[47], is calculated by:

$$MCR = \mathrm{dm}/(\mathrm{dQ}/-96{,}500) \quad (2)$$

where dm (g) is the differential mass change of the electrode and dQ is the differential charge change (C). From the slope of the linear region in Fig. 3c, MCR has the value of 22.4 g/mol e^-, close to the molar mass of Na^+. The slightly smaller value might be due to the partial participation of H_3O^+ with Na^+ in the electrochemical charge compensation process. The results indicate that, owing to the open layered structure of δ-MnO_2, electrolyte cations, mainly Na^+, could migrate rapidly into/out of the actuating material during potential scanning, while anions such as SO_4^{2-} do not participate in the actuation process, as sulfur cannot be found in the actuating material from the EDS mapping in Fig. S3. As shown in Fig. 3d, the binding energies at the Mn 2p XPS peaks are slightly higher in the oxidized state than those in the reduced state, which is likely due to a redox process taking place with a higher Mn valence in the oxidized state than that in the reduced state[70,75]. In Fig. 3e, the O 1s peaks can be deconvoluted into three components, namely, Mn-O-Mn bond (529.7‑529.8 eV) for the tetravalent oxide, Mn-OH bond (531.0-531.1 eV) for the hydrated trivalent oxide, and H-O-H bond (531.9-532.2 eV) for the residual structural water[70,76]. A distinct intensity shoulder on the higher binding side of the main peak is observed for the reduced sample, corresponding to the enhanced contribution of Mn-OH bond, indicating the change of the manganese oxide oxidation state between the oxidized and reduced state. The average oxidation state (AOS) of Mn species can be calculated by[70]:

$$\mathrm{AOS} = \frac{\mathrm{IV}*(S_{\mathrm{Mn-O-Mn}} - S_{\mathrm{Mn-OH}}) + \mathrm{III}* S_{\mathrm{Mn-OH}}}{S_{\mathrm{Mn-O-Mn}}} \quad (3)$$

where S stands for the signals of the different components of the O 1s spectra. According to the deconvoluted data in Table S2, The AOS is calculated to be 3.5 and 4.0, at the reduced and oxidized states, respectively. The GIXRD results of δ-MnO_2 in Figs. 3f and 3g clearly reveal the lengthening of d_{100} and d_{110} spacings in the reduced state compared with the oxidized counterpart. This is probably due to the Jahn-Teller distortion caused by Mn^{3+}. Also, the increased peak intensities for the oxidized state indicate the enhanced crystallinity of the

actuating material, as a result of the de-intercalation of interlayer species such as Na^+. The results here correspond well to the volume contraction of δ-MnO_2 in the oxidized state, and vice versa, as shown in Fig. 2b.

To summarize, during positive potential scanning, a redox pseudocapacitive process takes place in the δ-MnO_2 active layer, with the continuous oxidation of Mn species from the trivalent to tetravalent state and the de-intercalation of Na^+ from the active layer to the electrolyte, causing the shortening of d_{100} and d_{110} interplanar spacings and the enhanced crystallinity of the active material. Such structural changes lead to the overall volume contraction of the active layer, and eventually the forward curling of the δ-MnO_2/Ni actuator. The reverse process happens during negative potential scanning, causing the backward curling of the actuator.

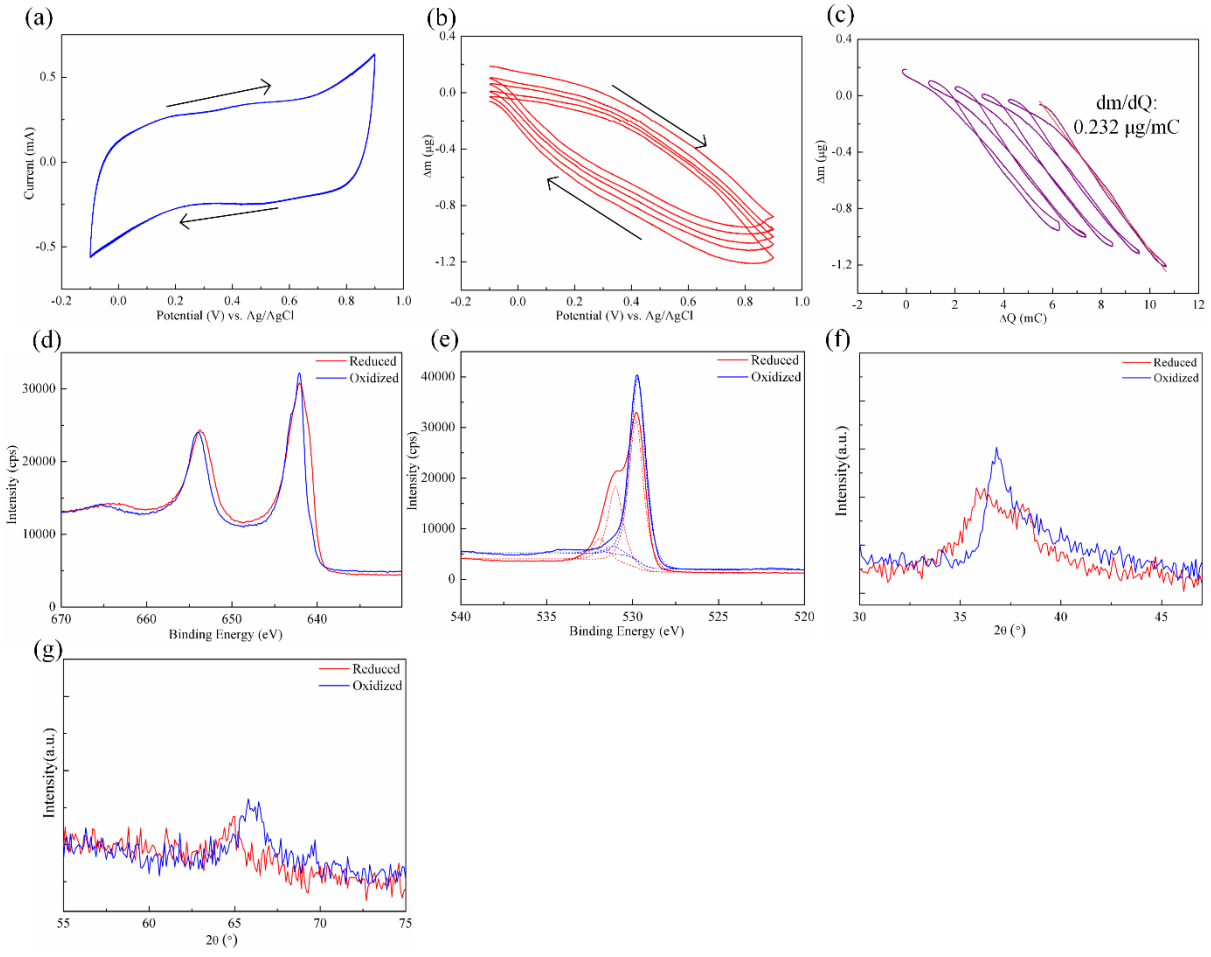

Fig. 3 (a) Cyclic voltammogram of δ-MnO_2 at scan rate of 0.05 V/s. The area of electrode is 0.196 cm^2. (b) Mass change of δ-MnO_2 at scan rate of 0.05 V/s. (c) Mass change of δ-MnO_2 versus charge change during potential scan. (d, e) Mn 2p (d) and O 1s (e) XPS spectra of δ-MnO_2 at oxidized and reduced states. (f, g) Enlarged views of (100) peaks (f) and of (110) peaks (g) of δ-MnO_2 at oxidized and reduced states.

Electrochemo-mechanical modelling of equilibrium actuation

Although the actuation performance and mechanism of δ-MnO_2/Ni actuators are investigated in detail above, a quantitative description on how their bending actuation in the steady state depends on the thermodynamic conditions of the electrochemical reaction has yet to be established. According to Fig. 2f, the actuation magnitude decreases as the potential scan rate u increases, and for $u \geqslant 0.4$ V/s, the $u^{-1/2}$ dependence according to the Randles–Sevcik equation[63,64] is obeyed, indicating that ionic diffusion in the electrolyte becomes rate-limiting for fast scan rates. On the other hand, as u decreases, the actuation magnitude rises towards a steady value as shown in Fig. 2f, indicative of an equilibrium condition for the actuation. Here, to model this equilibrium actuation condition for the δ-MnO_2/Ni actuators, we employ a recently developed model for bilayered-cantilever actuators that are surface stimulated, but modify it to suit the present redox mechanism[6,77].

Mechanics characteristics – the δ-MnO_2 active layer contracts upon oxidation and expands upon reduction, while the passive Au-Ni substrate remains unchanged in the process. The mismatch in length between the two layers causes the forward and backward curling of the actuator, as shown in Fig. 4a. Since the intermediate Au layer is ultrathin (~200 nm) and highly porous, the rigidity of this layer is ignored for simplicity. Besides, the δ-MnO_2 layer is relatively thin (~several microns); hence, in the oxidized (0.8 V vs SCE) and reduced (-0.2 V vs SCE)

equilibrium states, we assume that the actuating layer has uniform intrinsic strains ε_o and ε_r versus the neutral state, respectively, if detached from the substrate.

According to Timoshenko's strain-mismatch theory[34,78], the average stress in the oxidized and reduced states in the actuating layer, $\bar{\sigma}_o$ and $\bar{\sigma}_r$ respectively, are given by:

$$\bar{\sigma}_o = \frac{E_a h_a^3 + E_s h_s^3}{6h_a(h_a+h_s)} \kappa_o \tag{4}$$

$$\bar{\sigma}_r = \frac{E_a h_a^3 + E_s h_s^3}{6h_a(h_a+h_s)} \kappa_r \tag{5}$$

where E_a and E_s are the elastic moduli of the active layer and substrate, h_a and h_s are the thicknesses of the two layers, and κ_o and κ_r are the actuation curvatures in the oxidized and reduced state, respectively. Therefore, the change in the average actuation stress from the reduced state to the oxidized state, $\bar{\sigma}_a$, is given by:

$$\bar{\sigma}_a = \bar{\sigma}_o - \bar{\sigma}_r = \frac{E_a h_a^3 + E_s h_s^3}{6h_a(h_a+h_s)} (\kappa_o - \kappa_r) = \frac{E_a h_a^3 + E_s h_s^3}{6h_a(h_a+h_s)} \Delta\kappa \tag{6}$$

where $\Delta\kappa = \kappa_o - \kappa_r$ is the curvature change of the actuator from the reduced state to the oxidized state. On the other hand, the intrinsic oxidation strain ε_o and reduction strain ε_r are given as[6,77]:

$$\varepsilon_o = -\left[\frac{1}{E_a} + \frac{h_a}{E_s h_s} + \frac{3h_a(h_a+h_s)^2}{E_a h_a^3 + E_s h_s^3}\right] \bar{\sigma}_o \tag{7}$$

$$\varepsilon_r = -\left[\frac{1}{E_a} + \frac{h_a}{E_s h_s} + \frac{3h_a(h_a+h_s)^2}{E_a h_a^3 + E_s h_s^3}\right] \bar{\sigma}_r \tag{8}$$

and so, the total intrinsic actuation strain on going from the reduced state to the oxidized state, ε_a, is given by:

$$\varepsilon_a = \varepsilon_o - \varepsilon_r = -\left[\frac{1}{E_a} + \frac{h_a}{E_s h_s} + \frac{3h_a(h_a+h_s)^2}{E_a h_a^3 + E_s h_s^3}\right] \bar{\sigma}_a \tag{9}$$

Since the actuation mechanism of Na intercalation/de-intercalation discussed above happens at the surface of the active layer in contact with the electrolyte, the surface stress of the active layer is of special interest, as it would affect the equilibrium of the electrochemical processes

there. Thus, the stress of the active layer at the electrolyte interface region in the oxidized and reduced states is given by:

$$\sigma_o = \bar{\sigma}_o - \frac{E_a\, h_a}{2}\,\kappa_o = \left[\frac{E_a h_a^3 + E_s h_s^3}{6h_a(h_a+h_s)} - \frac{E_a\, h_a}{2}\right]\kappa_o \tag{10}$$

$$\sigma_r = \bar{\sigma}_r - \frac{E_a\, h_a}{2}\,\kappa_r = \left[\frac{E_a h_a^3 + E_s h_s^3}{6h_a(h_a+h_s)} - \frac{E_a\, h_a}{2}\right]\kappa_r \tag{11}$$

and so the change in the surface stress of the active layer between the oxidized and reduced states, σ_a, is given by:

$$\sigma_a = \sigma_o - \sigma_r = \left[\frac{E_a h_a^3 + E_s h_s^3}{6h_a(h_a+h_s)} - \frac{E_a\, h_a}{2}\right]\Delta\kappa \tag{12}$$

Therefore, the relation between σ_a and ε_a from Eqns. 6, 9 and 12 is:

$$\varepsilon_a = -C_a\sigma_a \tag{13}$$

where

$$C_a = \left[\frac{(h_a+h_s)}{2} + \frac{E_a h_a^3 + E_s h_s^3}{6(h_a+h_s)}\left(\frac{1}{E_a h_a} + \frac{1}{E_s h_s}\right)\right] \Big/ \left[\frac{E_a h_a^3 + E_s h_s^3}{6h_a(h_a+h_s)} - \frac{E_a\, h_a}{2}\right] \tag{14}$$

Electrochemical characteristics – The reversible actuation motion of a δ-MnO_2/Ni actuator is caused by a reversible electrochemical reaction which may be written as:

$$MnO_2(\text{smaller}) + Na^+ + e^- \rightleftharpoons MnOONa(\text{larger})$$

Switching the applied potential on the actuator could trigger a shift of the equilibrium of the above reaction and hence a volume change of the actuating layer. That is to say, the volumetric change of the actuating layer, namely, the intrinsic oxidation or reduction strain ε_o or ε_r ($\ll 1$), is a good indicator of equilibrium of the electrochemical reaction. Therefore, with reference to the neutral state where the intrinsic strain is zero, the electrochemical equilibrium constant at the δ-MnO_2-electrolyte interface can be expressed as:

$$(1+\varepsilon_o)^3 \approx (1+3\varepsilon_o) = K_{eq}^o = \exp\left(-\frac{\Delta E_o - \sigma_o\Omega}{k_B T}\right) \tag{15}$$

$$(1+\varepsilon_r)^3 \approx (1+3\varepsilon_r) = K_{eq}^r = \exp\left(-\frac{\Delta E_r - \sigma_r\Omega}{k_B T}\right) \tag{16}$$

where ΔE_o and ΔE_r are the electrochemical driving force arising from the oxidation and reduction potential bias relative to the zero-strain neutral potential, Ω is the activation volume, and k_B is Boltzmann's constant. Rearranging Eqns. 15 and 16, gives:

$$\sigma_o \Omega = \Delta E_o + k_B T \ln(1 + 3\varepsilon_o) \approx \Delta E_o + 3k_B T \varepsilon_o \tag{17}$$

$$\sigma_r \Omega = \Delta E_r + k_B T \ln(1 + 3\varepsilon_r) \approx \Delta E_r + 3k_B T \varepsilon_r \tag{18}$$

Combining Eqns. 17 and 18 gives:

$$\sigma_a \Omega = \Delta E_p + 3k_B T \varepsilon_a \tag{19}$$

where $\Delta E_p = \Delta E_o - \Delta E_r$ is the electrochemical driving force related to the applied potential.

Electrochemo-mechanics equilibrium – Eqns. 13 and 19 are satisfied concurrently when the electrode-electrolyte interface is at equilibrium, which leads to a solution for $(\sigma_a, \varepsilon_a)$. Thus, by substituting σ_a with $\Delta\kappa$ using Eqn. 12, the actuation curvature change $\Delta\kappa$ can be expressed in a normalized form as[6,77]:

$$\Delta K \coloneqq \frac{\Delta\kappa h_s}{\phi\beta^{1/3}} = \frac{6\alpha\beta^{2/3}(1+\alpha)}{(1+\alpha\beta)(1+\alpha^3\beta)+\omega[1-\alpha^2\beta(3+2\alpha)]+3\alpha\beta(1+\alpha)^2} \tag{20}$$

where $\alpha = h_a/h_s$, $\beta = E_a/E_s$, $\phi = \Delta E_p/(3k_B T)$ and $\omega = E_a\Omega/(3k_B T)$. The normalized curvature change ΔK is a comprehensive index of the actuator performance, including the factors of the substrate bending stiffness $E_s h_s^3$ and the electrochemical potential driving force ΔE_p. That is to say, a larger ΔK may stem from a larger actuation curvature $\Delta\kappa$, or the same actuation curvature on a substrate with a larger bending stiffness $E_s h_s^3$, or the same actuation curvature on the same substrate but with a smaller electrochemical potential window. ϕ and ω are normalized measures for the electrochemical potential driving force ΔE_p, and the activation volume Ω. Note that Eqn. 19 can be written in the form:

$$\varepsilon_a = \left(\frac{\sigma_a}{E_a}\right)\omega - \phi \tag{21}$$

Thus, ϕ and ω values can be estimated from the slope and y-intercept by plotting ε_a against σ_a/E_a using experimental data.

Intrinsic actuation properties of δ-MnO_2

To quantify the intrinsic actuation properties of actuating material, actuators with different actuating layer thicknesses (from 0.74 to 4.43 μm) but the same substrate thickness of 1.35 ± 0.15 μm were fabricated and tested using step-potential change between -0.2 and 0.8 V vs SCE at temperatures T = 288, 298 and 313 K. The steady-state actuation after the step-potential change was used in the analysis. Young's moduli of the actuating layer and Ni substrate are measured to be 33.7±9.0 and 182.5±13.1 GPa, respectively. Different actuation parameters, including $\Delta\kappa$, $\bar{\sigma}_a$, σ_a, σ_s and ε_a, are calculated accordingly from the steady-state actuation and plotted against h_a for analysis. In Fig. 4b, the actuation curvature change $\Delta\kappa$ increases rapidly with h_a before $h_a = 2.3$ μm, and reaches the maximum value of 3.80×10^3 m^{-1} at $h_a = 3.5$ μm, followed by a drop at larger h_a. This is because for small h_a, the actuation of the actuators tends to be bending-dominated, where increasing h_a would offer a larger actuation force to bend against the rigidity of the substrate, therefore giving rise to larger $\Delta\kappa$. However, when the actuating layer is significantly thicker than the substrate, the actuation will become stretching-dominated, where a thicker active layer simply stretches the substrate instead of bending it, and so $\Delta\kappa$ increases slowly or eventually drops. Fig. 4c shows the change in the average actuation stress $\bar{\sigma}_a$, and the change in the stress at the actuating layer-electrolyte interface σ_a plotted against h_a, according to Eqns. 6 and 12. From the graph, $\bar{\sigma}_a$ is always tensile and shows an overall mild increasing trend from 36.8 to 71.5 MPa in the h_a range studied. However, with the increase of h_a in the same range, σ_a, which shows an opposite trend with $\bar{\sigma}_a$, is tensile at small h_a and turns into compressive with $h_a > 1.8$ μm. The results show that, when h_a is small, the value of σ_a is highly dependent on $\bar{\sigma}_a$, while at large h_a, mechanical

bending stress plays the dominant role in determining its value. In Fig. 4d, the absolute value of the total intrinsic actuation strain ε_a increases steadily with h_a in the region studied according to Eqns. 6 and 9, with the maximum value of 1.28% at $h_a = 4.4$ μm. From the red symbols in Fig. 4e, the experimentally obtained ε_a and σ_a/E_a show good linearity according to the electrochemical characteristics in Eqn. 21, thus giving the estimates of $\phi = 4.37 \times 10^{-3}$ and $\omega = 1.71$, corresponding to $\Delta E_p = 5.39 \times 10^{-23}$ J and $\Omega = 6.26 \times 10^{-31}$ m^3, respectively, at T = 298 K. Furthermore, the same tests were conducted under the temperatures of 288 and 313K and the data are presented as green and blue symbols in Fig. 4e. Good linearity between ε_a and σ_a/E_a is also observed, which gives $\Delta E_p = 4.08 \times 10^{-23}$ J, $\Omega = 6.83 \times 10^{-31}$ m^3 at T = 288 K, and $\Delta E_p = 6.94 \times 10^{-23}$ J, $\Omega = 6.38 \times 10^{-31}$ m^3 at T = 313 K (Table 1). The data clearly show that increasing temperature can significantly enhance the electrochemical driving force ΔE_p, with little variation in the activation volume Ω. The theoretical relations between the actuation curvature change and actuating layer thickness at different actuation temperatures are therefore determined in the normalized forms by Eqn. 21 and shown in Fig. 4f. The discrete symbols, representing the experimental data, correlate well with the theoretical curves at different temperatures. The results clearly show that the electrochemo-mechanical model is quantitively accurate for describing the electrochemical actuation behavior of δ-MnO_2/Ni bilayered actuators at different temperatures.

From the modelling data, at room temperature of 298 K, the δ-MnO_2 actuating material has the maximum actuation strain of 1.28%, which outperforms other transition-metal oxides/hydroxides materials[16,17] (~0.1%), carbon based materials[26,29,30] and noble metals[22,23]. Though the actuation strain of δ-MnO_2 is lower than that of conducting polymers, the change in the average actuation stress (71.5 MPa) under the electrochemical stimuli is much larger than its polymeric counterparts[79,80], owing to the high strength and stiffness of the material. The peak actuation strain rate of the material obtained from Fig. 2c using Eqns. 12 and 13 is

0.46% s^{-1}. The maximum actuation work density of the δ-MnO_2 actuating material is calculated as $W = 0.5\ E_a\varepsilon_a^2$ to be 2.76 MJ/m^3, which far outperforms that of human skeletal muscles[1] and other actuating material counterparts[17,81]. All in all, these actuating parameters clearly reveal that δ-MnO_2 is a promising artificial-muscle material for developing miniaturized electrochemical actuators.

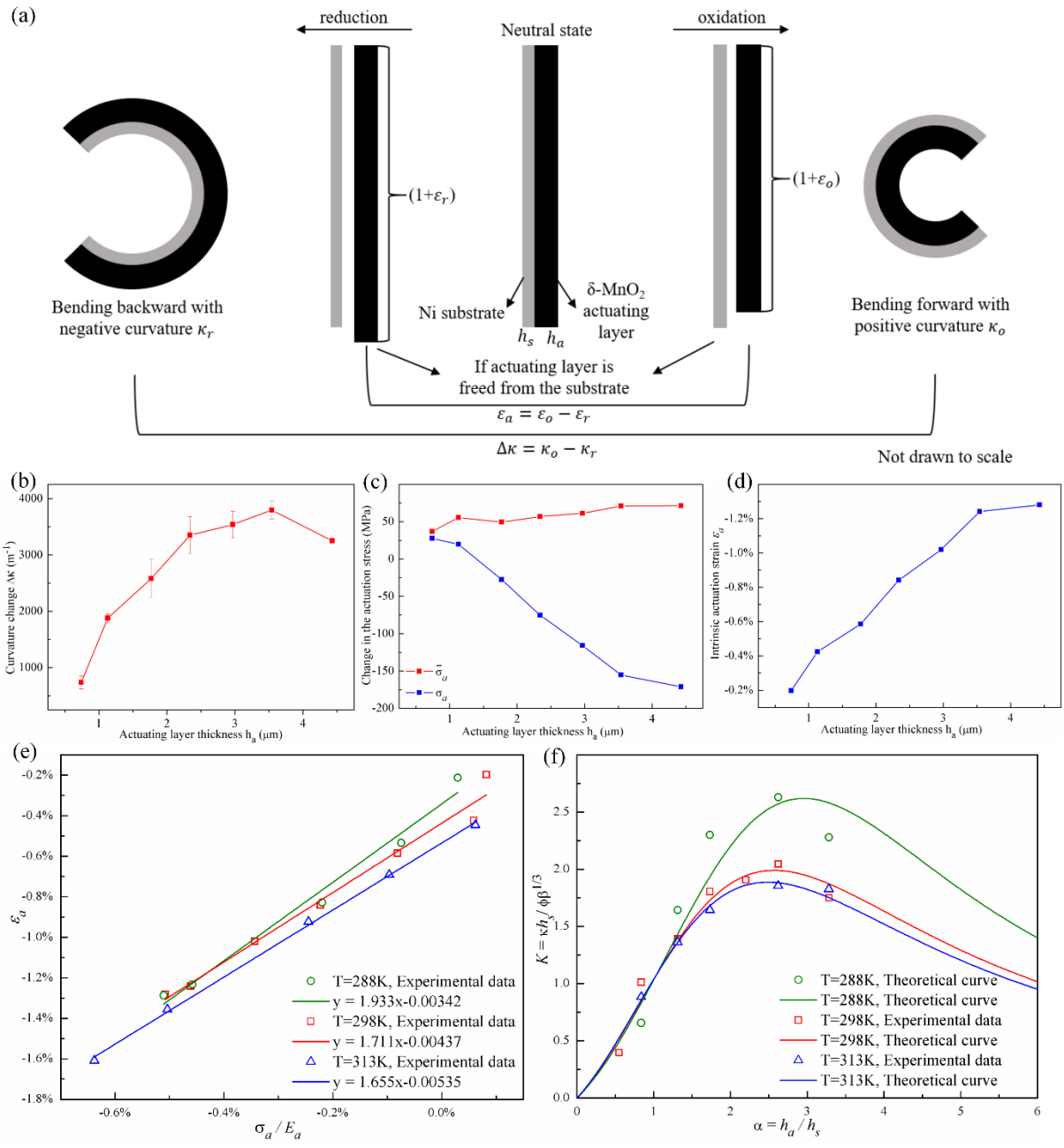

Fig. 4 (a) Schematic of the electrochemical actuation of the bilayered actuator. (b)

Electrochemical actuation curvature change κ plotted against h_a at T=298 K. (c) Change in the average actuation stress $\bar{\sigma}_a$, and actuating layer-electrolyte interface stress σ_a plotted against h_a at T=298 K. (d) Intrinsic actuation strain ε_a plotted against h_a at T=298 K. (e) Linear fitting of ε_a and $\frac{\sigma_a}{E_a}$ at different temperatures. (f) The normalized curvature change ΔK plotted against α at different temperatures.

Temperature (K)	288	298	313
ϕ	$(3.42 \pm 0.46) \times 10^{-3}$	$(4.37 \pm 0.32) \times 10^{-3}$	$(5.35 \pm 0.12) \times 10^{-3}$
ΔE_p (J)	$(4.08 \pm 0.55) \times 10^{-23}$	$(5.39 \pm 0.40) \times 10^{-23}$	$(6.94 \pm 0.16) \times 10^{-23}$
ω	1.93 ± 0.14	1.71 ± 0.11	1.66 ± 0.03
Ω (m^3)	$(6.83 \pm 0.50) \times 10^{-31}$	$(6.26 \pm 0.40) \times 10^{-31}$	$(6.38 \pm 0.12) \times 10^{-31}$

Table 1 – ϕ, ΔE_p, ω and Ω at different temperatures.

Applications of δ-MnO_2 actuators

As the δ-MnO_2 actuators are fabricated by electrodeposition, their shapes and thicknesses can be designed to realize various motions and functions. Here, we designed two devices to illustrate the versatility of the δ-MnO_2 actuators. First, a strip-shaped fish hook was fabricated by electrodepositing δ-MnO_2 onto an MPPC substrate[33]. The object catching capability of this device is shown in Video S3, Supporting Information. The hook is at reduced state initially, as shown in Fig. 5a, and by adjusting the potential to a positive value, the hook bends reversely and catches the yellow object, as shown in Fig. 5b. The result shows the adaptability of the δ-MnO_2 actuating material on different substrates with proper functionality. Furthermore, an accordion-like linear actuator was fabricated by selective deposition of δ-MnO_2 on both sides of a Ni thin-film substrate, as shown in Fig. 5c, and the actuation performance is shown in Video S4, Supporting Information. At the reduced state, the actuating material is expanded,

causing the curling of the hinges on the actuator and thus contraction of the actuator. Upon oxidation, along with the continuous contraction of the actuating material on both sides, the accordion-like actuator straightens first, to its maximum length, and then the hinges on the actuator curls reversely, rendering the re-contraction of the actuator. The linear actuator can generate an extremely large device strain of 300%, as shown in Figs. 5d and e. The two examples demonstrate the potential and maneuverability of δ-MnO_2 for developing electrochemical actuators.

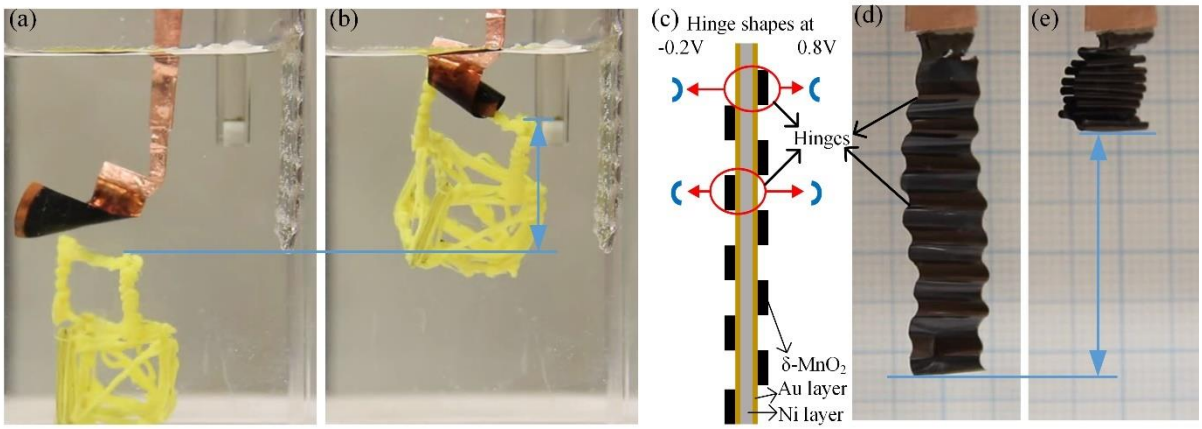

Fig. 5 (a, b) Fish hook actuator at the reduced state (a) and oxidized state (b). (c) Schematic of the accordion-like actuator and the corresponding hinge shapes at -0.2 and 0.8 V. (d, e) Accordion-like actuator at the stretched state (d) and contracted state (e).

Conclusions

In this work, we reported the high-performing electrochemical actuation behavior of *c*-disordered δ-MnO_2 for the first time, and fabricated bilayered δ-MnO_2/Ni electrochemical actuators with excellent actuation performances under the electrical stimuli below 1V. The actuation magnitude and speed of the actuators are linearly controllable by adjusting the electrochemical potential scan window and rate. The actuation stems from the volumetric change in the δ-MnO_2 material by Mn^{3+}/Mn^{4+} redox transition and fast intercalation/de-

intercalation of sodium ions upon potential variations. An electrochemo-mechanical model was applied to quantitatively capture the intrinsic actuation properties of δ-MnO_2, as well as the macroscopic actuation performance of their bilayered actuators. The theoretical predictions of the actuation correlate well with the experimental observations of actuation magnitudes at different temperatures, reflecting the validity of the model. Based on the model, the *c*-disordered δ-MnO_2 actuating material has a maximum actuation strain of 1.28%, average actuation stress of 71.5 MPa, peak strain rate of around 0.46% s^{-1}, and a maximum actuation energy density of 2.76 MJ/m^3. The results clearly indicate that δ-MnO_2 is a promising actuating material for developing miniaturized robotic devices.

Author Contributions

Wenrui Ma: Conceptualization, Methodology, Investigation: performing the experiments on actuator development, materials and mechanisms characterization, and data collection, Formal analysis, Writing: original draft. **Kin Wa Kwan**: Conceptualization, Methodology, Investigation: performing the experiments on actuator development, Validation, Writing: review & editing. **Runni Wu**: Methodology. **Alfonso H.W. Ngan**: Conceptualization, Funding acquisition, Supervision, Writing: review & editing.

Conflicts of Interest

The authors declare no conflicts of interest.

Acknowledgements

This work was supported by the Kingboard Endowed Professorship in Materials Engineering. The authors are grateful to Mr. F.Y.F Chan for assistance in TEM, and Dr. S.P. Feng and Ms. K. Mu for their assistance in the EQCM measurements.

References

1 J. D. W. Madden, N. A. Vandesteeg, P. A. Anquetil, P. G. A. Madden, A. Takshi, R. Z. Pytel, S. R. Lafontaine, P. A. Wieringa and I. W. Hunter, 2004, **29**, 706–728.

2 Q. Zhao, J. Heyda, J. Dzubiella, K. Täuber, J. W. C. Dunlop and J. Yuan, *Adv. Mater.*, 2015, **27**, 2913–2917.

3 J. M. Hollerbach, I. M. Hunter and J. Ballentyne, in *The Robotics Review 2*, 1991.

4 J. Song and Y. Zhang, *Chem. Eng. J.*, 2019, **360**, 680–685.

5 C. Wang, Y. Wang, Y. Yao, W. Luo, J. Wan, J. Dai, E. Hitz, K. K. Fu and L. Hu, *Adv. Mater.*, 2016, **28**, 8618–8624.

6 K. W. Kwan and A. H. W. Ngan, *Adv. Mater. Technol.*, 2019, **4**, 1900746.

7 K. W. Kwan, S. J. Li, N. Y. Hau, W.-D. Li, S. P. Feng and A. H. W. Ngan, *Sci. Robot.*, 2018, **3**, eaat4051.

8 M. Rogóż, H. Zeng, C. Xuan, D. S. Wiersma and P. Wasylczyk, *Adv. Opt. Mater.*, 2016, **4**, 1689–1694.

9 M. Ji, N. Jiang, J. Chang and J. Sun, *Adv. Funct. Mater.*, 2014, **24**, 5412–5419.

10 B. Shin, J. Ha, M. Lee, K. Park, G. H. Park, T. H. Choi, K. J. Cho and H. Y. Kim, *Sci. Robot.*, 2018, **3**, 1–9.

11 M. Dai, O. T. Picot, J. M. N. Verjans, L. T. De Haan, A. P. H. J. Schenning, T. Peijs and C. W. M. Bastiaansen, *ACS Appl. Mater. Interfaces*, 2013, **5**, 4945–4950.

12 H. Arazoe, D. Miyajima, K. Akaike, F. Araoka, E. Sato, T. Hikima, M. Kawamoto and T. Aida, *Nat. Mater.*, 2016, **15**, 1084–1089.

13 P. Brochu and Q. Pei, *Macromol. Rapid Commun.*, 2010, **31**, 10–36.

14 B. Chen, J. J. Lu, C. H. Yang, J. H. Yang, J. Zhou, Y. M. Chen and Z. Suo, *ACS Appl. Mater. Interfaces*, 2014, **6**, 7840–7845.

15 S. Q. Wang, B. Zhang, X. M. Luo, F. Liang and G. P. Zhang, *J. Mater. Chem. A*, 2020, **8**, 5679–5687.

16 K. W. Kwan, N. Y. Hau, S. P. Feng and A. H. W. Ngan, *Sensors Actuators, B Chem.*, 2017, **248**, 657–664.

17 L. Liu, L. Su, Y. Lu, Q. Zhang, L. Zhang, S. Lei, S. Shi, M. D. Levi and X. Yan, *Adv. Funct. Mater.*, 2019, **29**, 1–12.

18 C. Cheng and A. H. W. Ngan, *ACS Nano*, 2015, **9**, 3984–3995.

19 M. Fuchiwaki, J. G. Martinez and T. F. Otero, *Electrochim. Acta*, 2016, **195**, 9–18.

20 F. García-Córdova, L. Valero, Y. A. Ismail and T. F. Otero, *J. Mater. Chem.*, 2011, **21**, 17265–17272.

21 U. L. Zainudeen, M. A. Careem and S. Skaarup, *Sensors Actuators, B Chem.*, 2008, **134**, 467–470.

22 J. Weissmüller, R. N. Viswanath, D. Kramer, P. Zimmer, R. Würschum and H. Gleiter, *Science (80-.).*, 2003, **300**, 312–315.

23 E. Detsi, M. S. Sellès, P. R. Onck and J. T. M. De Hosson, *Scr. Mater.*, 2013, **69**, 195–198.

24 H. J. Jin, X. L. Wang, S. Parida, K. Wang, M. Seo and J. Weissmüller, *Nano Lett.*, 2010, **10**, 187–194.

25 R. H. Baughman, C. Cui, A. A. Zakhidov, Z. Iqbal, J. N. Barisci, G. M. Spinks, G. G. Wallace, A. Mazzoldi, D. De Rossi, A. G. Rinzler, O. Jaschinski, S. Roth and M. Kertesz, *Science (80-.).*, 1999, **284**, 1340–1344.

26 M. Hughes and G. M. Spinks, *Adv. Mater.*, 2005, **17**, 443–446.

27 J. A. Lee, N. Li, C. S. Haines, K. J. Kim, X. Lepró, R. Ovalle-Robles, S. J. Kim and R. H. Baughman, *Adv. Mater.*, 2017, **29**, 1–7.

28 J. Liang, L. Huang, N. Li, Y. Huang, Y. Wu, S. Fang, J. Oh, M. Kozlov, Y. Ma, F. Li, R. Baughman and Y. Chen, *ACS Nano*, 2012, **6**, 4508–4519.

29 G. W. Rogers and J. Z. Liu, *J. Am. Chem. Soc.*, 2011, **133**, 10858–10863.

30 X. Xie, L. Qu, C. Zhou, Y. Li, J. Zhu, H. Bai, G. Shi and L. Dai, *ACS Nano*, 2010, **4**, 6050–6054.

31 C. Cheng, J. Weissmüller and A. H. W. Ngan, *Adv. Mater.*, 2016, **28**, 5315–5321.

32 K. W. Kwan and A. H. W. Ngan, *ACS Appl. Mater. Interfaces*, 2020, **12**, 30557–30564.

33 R. Wu, K. W. Kwan, W. Ma, P. Wang and A. H. W. Ngan, *Appl. Mater. Today*, 2020, **20**, 1–14.

34 K. W. Kwan and A. H. W. Ngan, *Adv. Mater. Technol.*, 2019, **4**, 1–8.

35 R. H. Baughman, *Science (80-.).*, 2003, **300**, 268–269.

36 C. Cheng and A. H. W. Ngan, *Appl. Phys. Lett.*, , DOI:10.1063/1.4808212.

37 D. Wang, L. Wang, G. Liang, H. Li, Z. Liu, Z. Tang, J. Liang and C. Zhi, *ACS Nano*, 2019, **13**, 10643–10652.

38 S. Devaraj and N. Munichandraiah, *J. Phys. Chem. C*, 2008, **112**, 4406–4417.

39 S. Komaba, N. Kumagai and S. Chiba, *Electrochim. Acta*, 2000, **46**, 31–37.

40 Y. Matsuo, Y. Miyamoto, T. Fukutsuka and Y. Sugie, *J. Power Sources*, 2005, **146**, 300–303.

41 M. Tsuda, H. Arai and Y. Sakurai, *J. Power Sources*, 2002, **110**, 52–56.

42 M. Feng, Q. Du, L. Su, G. Zhang, G. Wang, Z. Ma, W. Gao, X. Qin and G. Shao, *Sci. Rep.*, 2017, **7**, 1–8.

43 L. Athouël, F. Moser, R. Dugas, O. Crosnier, D. Bélanger and T. Brousse, *J. Phys.*

Chem. C, 2008, **112**, 7270–7277.

44 Y. Zhao, Q. Fang, X. Zhu, L. Xue, M. Ni, C. Qiu, H. Huang, S. Sun, S. Li and H. Xia, *J. Mater. Chem. A*, 2020, **8**, 8969–8978.

45 M. Pang, G. Long, S. Jiang, Y. Ji, W. Han, B. Wang, X. Liu and Y. Xi, *Electrochim. Acta*, 2015, **161**, 297–304.

46 G. Sauerbrey, *Zeitschrift für Phys.*, 1959, **155**, 206–222.

47 S.-L. Kuo and N.-L. Wu, *J. Electrochem. Soc.*, 2006, **153**, A1317.

48 V. A. Drits, E. Silvester, A. I. Gorshkov and A. Manceau, *Am. Mineral.*, 1997, **82**, 946–961.

49 R. Kavian, A. Vicenzo and M. Bestetti, *J. New Mater. Electrochem. Syst.*, 2015, **18**, 43–48.

50 A. Cormie, A. Cross, A. F. Hollenkamp and S. W. Donne, *Electrochim. Acta*, 2010, **55**, 7470–7478.

51 S. Komaba, A. Ogata and T. Tsuchikawa, *Electrochem. commun.*, 2008, **10**, 1435–1437.

52 M. Villalobos, B. Toner, J. Bargar and G. Sposito, *Geochim. Cosmochim. Acta*, 2003, **67**, 2649–2662.

53 H. Zhao, X. Liang, H. Yin, F. Liu, W. Tan, G. Qiu and X. Feng, *Geochem. Trans.*, 2015, **16**, 1–11.

54 M. Villalobos, B. Lanson, A. Manceau, B. Toner and G. Sposito, *Am. Mineral.*, 2006, **91**, 489–502.

55 A. L. Atkins, S. Shaw and C. L. Peacock, *Geochim. Cosmochim. Acta*, 2014, **144**, 109–125.

56 J. E. Post and D. R. Veblen, *Am. Mineral.*, 1990, **75**, 477–489.

57 J. Yan, Z. Fan, T. Wei, W. Qian, M. Zhang and F. Wei, *Carbon N. Y.*, 2010, **48**, 3825–

3833.

58 Y. Li, Z. Xu, D. Wang, J. Zhao and H. Zhang, *Electrochim. Acta*, 2017, **251**, 344–354.

59 X. Wang, S. Chen, D. Li, S. Sun, Z. Peng, S. Komarneni and D. Yang, *ACS Sustain. Chem. Eng.*, 2018, **6**, 633–641.

60 C. D. Wagner, W. M. Riggs, L. E. Davis, J. F. Moulder and G. E. Muilenberg, *Handbook of X-ray electron spectroscopy: A reference book of standard data for use in X-ray photoelectron spectroscopy*, 1979.

61 H. C. Genuino, S. Dharmarathna, E. C. Njagi, M. C. Mei and S. L. Suib, *J. Phys. Chem. C*, 2012, **116**, 12066–12078.

62 X. Zhang, S. Wu, S. Deng, W. Wu, Y. Zeng, X. Xia, G. Pan, Y. Tong and X. Lu, *Small Methods*, 2019, **3**, 1900525.

63 A. Ševčík, *Collect. Czechoslov. Chem. Commun.*, 1948, **13**, 349–377.

64 J. E. B. Randles, *Trans. Faraday Soc.*, 1948, **44**, 327–338.

65 W. Wei, X. Cui, W. Chen and D. G. Ivey, *Chem. Soc. Rev.*, 2011, **40**, 1697–1721.

66 S. Sopčić, R. Peter, M. Petravić and Z. Mandić, *J. Power Sources*, 2013, **240**, 252–257.

67 C. Tanggarnjanavalukul, N. Phattharasupakun, J. Wutthiprom, P. Kidkhunthod and M. Sawangphruk, *Electrochim. Acta*, 2018, **273**, 17–25.

68 S. R. Sivakkumar, J. M. Ko, D. Y. Kim, B. C. Kim and G. G. Wallace, *Electrochim. Acta*, 2007, **52**, 7377–7385.

69 M. Pourbaix, H. Zhang and A. Pourbaix, *Mater. Sci. Forum*, 1997, **251**–**254**, 143–148.

70 M. Toupin, T. Brousse and D. Bélanger, *Chem. Mater.*, 2004, **16**, 3184–3190.

71 S. C. Pang and M. A. Anderson, *J. Mater. Res.*, 2000, **15**, 2096–2106.

72 H. Y. Lee, V. Manivannan and J. B. Goodenough, *Comptes Rendus l'Academie des Sci. - Ser. IIc Chem.*, 1999, **2**, 565–577.

73 X. Shan, F. Guo, D. S. Charles, Z. Lebens-Higgins, S. Abdel Razek, J. Wu, W. Xu, W. Yang, K. L. Page, J. C. Neuefeind, M. Feygenson, L. F. J. Piper and X. Teng, *Nat. Commun.*, 2019, **10**, 1–11.

74 Z. Sun, Y. Zhang, Y. Liu, J. Fu, S. Cheng, P. Cui and E. Xie, *J. Power Sources*, 2019, **436**, 226795.

75 M. Chigane, M. Ishikawa and M. Izaki, *J. Electrochem. Soc.*, 2001, **148**, D96.

76 W. Chen, G. Li, A. Pei, Y. Li, L. Liao, H. Wang, J. Wan, Z. Liang, G. Chen, H. Zhang, J. Wang and Y. Cui, *Nat. Energy*, 2018, **3**, 428–435.

77 W. Ma, K. W. Kwan, R. Wu and A. H. W. Ngan, *Extrem. Mech. Lett.*, 2020, **39**, 100801.

78 S. Timoshenko, *J. Opt. Soc. Am.*, 1925, **11**, 233.

79 L. Bay, K. West, P. Sommer-Larsen, S. Skaarup and M. Benslimane, *Adv. Mater.*, 2003, **15**, 310–313.

80 C. V. Fengel, N. P. Bradshaw, S. Y. Severt, A. R. Murphy and J. M. Leger, *Smart Mater. Struct.*, 2017, **26**, 055004.

81 M. Acerce, E. K. Akdoan and M. Chhowalla, *Nature*, 2017, **549**, 370–373.